The following publication Cui, W., Li, J., Cen, W., Sun, Y., Lee, S. C., & Dong, F. (2017). Steering the interlayer energy barrier and charge flow via bioriented transportation channels in g-C3N4: enhanced photocatalysis and reaction mechanism. Journal of catalysis, 352, 351-360 is available at https://doi.org/10.1016/j.jcat.2017.05.017.

Graphical Abstract

Interlayer bi-oriented electrons transportation channels in KNO_3 co-doped CN could reduce the interlayer energy barrier, steer charge flow to promote charge separation and enhance the O_2 activation for superior visible-light photocatalytic performance in NO purification.

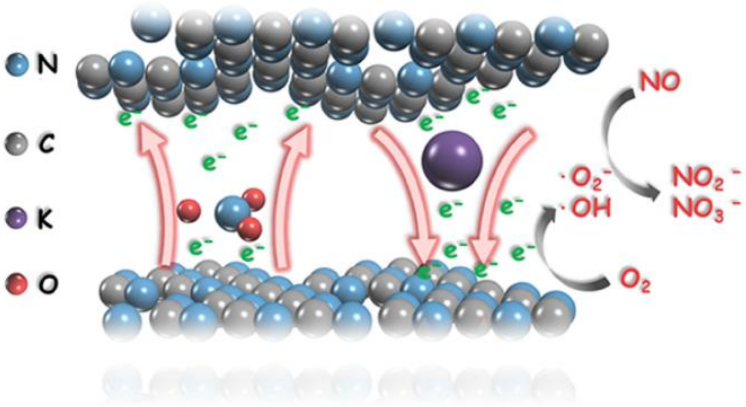

Highlights

- Interlayer bi-oriented electrons transportation channels in g-C_3N_4 were crafted.
- Interlayer energy barrier was reduced and charge separation was promoted.
- KNO_3 Co-doped g-C_3N_4 exhibited superior visible-light photocatalytic activity.
- A highly combined theoretical and experimental method was applied.
- The photocatalysis mechanism was elucidated *via* ESR and *in situ* DRIFTS.

Research highlights

We craft the interlayer bi-oriented electrons transportation channels via intercalation K^+ and NO_3^- species between the neighboring layers of g-C_3N_4. A highly combined theoretical and experimental method is proposed to demonstrate the construction of interlayer bi-oriented channels. The established bi-oriented channels could reduce the energy barrier for electrons transportation between adjacent layers and steer the charge flow towards opposite direction. The abundant electrons can be provided to activate O_2 molecule and thus dramatically facilitates the production of reactive species to participate in the photocatalytic redox reaction. The reduced energy barrier, promoted charge separation and transportation, and enhanced O_2 activation in all endow the KNO_3 co-doped g-C_3N_4 superior visible-light photocatalytic performance in NO purification. The conversion pathway of photocatalytic NO oxidation and photocatalytic promotion mechanism are proposed.

Steering the interlayer energy barrier and charge flow *via* bi-oriented transportation channels in g-C_3N_4: enhanced photocatalysis and reaction mechanism

Wen Cui [a,⊥], Jieyuan Li [b,⊥], Wanglai Cen [b], Yanjuan Sun [a], S. C. Lee [c], Fan Dong [*,a]

[a] Chongqing Key Laboratory of Catalysis and New Environmental Materials, College of Environment and Resources, Chongqing Technology and Business University, Chongqing 400067, P. R. China.

[b] Institute of New Energy and Low Carbon Technology, College of Architecture and Environment, Sichuan University, Chengdu, Sichuan 610065, P. R. China.

[c] Department of Civil and Environmental Engineering, The Hong Kong Polytechnic University, Hong Kong, China.

[⊥]These authors contribute equally to this work. (Wen Cui and Jieyuan Li)

*Corresponding Authors:

Prof. Fan Dong (dfctbu@126.com)

Abstract: Even though graphitic carbon nitride (g-C_3N_4, short for CN) is ideal for photocatalysis, the inherent defects that large interlayer energy barrier and low charge separation efficiency have limited the transportation and transformation of carriers. Here, we tackle these challenges to craft interlayer bi-oriented electrons transportation channels via intercalation K^+ and NO_3^- species between the neighboring layers of CN, lowering the interlayer energy barrier and driving the interlayer charge flow. A highly combined theoretical and experimental method is proposed to demonstrate the construction of interlayer bi-oriented channels in CN. The energy barrier of electrons transfer between adjacent layers observably decrease from -34.16 eV of CN to -28.17 eV of KNO_3 co-doped CN (short for CN-KN). The charge flow induced by the two channels could transfer towards opposite directions, resulting in the significantly boosted separation and transportation efficiency of carriers. Consequently, the abundant electrons can be provided to activate the O_2 molecule and thus dramatically facilitates the production of reactive species to participate in the photocatalytic redox reaction. The reduced energy barrier, promoted charge separation and transportation, and enhanced O_2 activation in all endow the CN-KN superior visible-light photocatalytic performance in NO purification. Besides, the conversion pathways of photocatalytic NO oxidation on CN and CN-KN have been elucidated and compared based on the ESR spectra and *in situ* DRIFTS spectra. A new absorption band at 2150 cm^{-1} associated with NO^+ intermediate is discovered for CN-KN. This research highlights the crucial issues in steering the interlayer energy barrier and charge flow *via* bi-oriented transportation channels to promote the separation, transportation and transformation efficiency of photogenerated carriers, and paves a new way to effectively elevate the photocatalytic performance of layered photocatalysts.

Keywords: Co-doped g-C_3N_4; Electron transportation channels; Charge separation and transportation; Visible light photocatalysis; Photocatalytic NO oxidation mechanism.

1. Introduction

Photocatalysis has received broad interests due to its promising applications in environmental pollution control and solar energy conversion [1-3]. Generally, the photocatalytic process involves three primary steps: (1) The absorption of light through semiconductor excitation to produce electrons/holes pairs; (2) The separation and transportation of photogenerated electrons and holes; (3) The photocatalytic redox reaction with the reactive radicals. Conceivably, the outstanding photocatalysts should be excited favorably and possess efficient separation, transportation and transformation efficiency of carriers [4-7].

Recently, two dimensional (2D) layered materials have been extensively explored and applied in photocatalysis, shedding new light on addressing the issues of environmental concerns and energy shortage [8-11]. Graphitic carbon nitride (g-C_3N_4, short for CN), a 2D semiconductor with graphitic planes consisting of sp^2 hybridized tri-s-triazine repeating units in planes and weak van der Waals force between layers, has become an attractive and hot photocatalyst due to the unique layered structure, tunable electronic band structure and fascinating physicochemical properties [12-15].

Unfortunately, limited by the chemically sluggish property originating from the intrinsic graphitic π-conjugated structure and weak covalence between layers, the photogenerated carriers would transfer randomly in planes and thus triggering low charge separation efficiency and unsatisfied photocatalytic performance [16-18]. Thus, various strategies including inner architecture modification and surface functionalization (elemental doping, microstructure design, and construction of

heterojunctions) have been developed for further optimization on CN performance [19, 20]. Given the fact that the layered CN has a large interlayer space of 0.324 nm and weak van der Waals force between adjacent layers [17, 21], sandwiching suitable candidates between contiguous layers to bridge the interlayers is a potentially feasible strategy that could overcome these obstacles by driving the carriers transfer between neighboring layers and thus promoting the charge separation efficiency. Recently, our group constructed K-intercalated CN to bridge the adjacent layers of CN and build an interlayer electrons delivery channel for the efficient separation and transportation of charges and the excellent photocatalytic activity [17]. While this strategy is effective, there is still much scope to improve the photocatalytic performance by further reducing the interlayer energy barriers for charge transportation and boosting the charge separation and transportation efficiency. Understandably, the metal/nonmetal co-doping in CN as an effective modification method is considerable, which could further promote the separation of photogenerated electrons and holes via the synergistic effect of metal/nonmetal co-doping [22, 23].

Herein, we firstly crafted the interlayer bi-oriented electrons transportation channels in CN *via* intercalation K and NO_3^- species between neighboring layers. The established bi-oriented channels could observably reduce the energy barrier for electrons transfer between adjacent layers and steer the charge flow towards opposite directions. The reversed channels constructed by the inset of KNO_3 have been demonstrated through the highly combined theoretical and experimental method. Correspondingly, the inevitable recombination of carriers which caused by the

accumulation of electrons in one layer through single channel transportation have been precluded and then the separation and transportation efficiency of carriers is significantly boosted via the special bi-oriented channels. Also, abundant electrons in the channels could serve for activating O_2 molecules to generate increased amount of reactive species. The reduced energy barrier, promoted charge separation and transportation, and enhanced O_2 molecule activation of CN-KN in all contributed to the highly enhanced visible-light photocatalytic performance in NO purification superior to pristine CN. The conversion pathways of photocatalytic NO oxidation on CN and CN-KN have been elucidated and compared based on the ESR spectra and *in situ* DRIFTS spectra. Finally, we highlight some critical issues in engineering the layered-structure mediated properties and steering the interlayer energy barrier and charge flow of CN *via* a desired and effective manner, which can provide alternative strategies to construct highly efficient layered photocatalysts.

2. Experiment and calculation

2.1 Catalysts Preparation

All chemicals employed in this study were analytical grade and were used without further treatment. And the CN-KN samples were synthesized *via* co-pyrolysis of thiourea and KNO_3. First, 10 g of thiourea and a known amount (1, 3, 5 wt %, relative to the experimentally obtained CN) of KNO_3 were added in an alumina crucible (50 mL) with 20 mL distilled water. The obtained solution was then dried at 80 °C to get the solid precursors. And then the solid composite precursor placed in a semi-closed

alumina crucible with a cover was calcined at 550 °C for 2 h with a heating rate of 15 °C/min in static air. After the thermal treatment, the crucible cooled down to room temperature and the obtained samples with different weight ratio (1, 3, and 5 wt %) were collected and labeled as CN-KN1, CN-KN3 and CN-KN5, respectively. For comparison, an ex-situ mechanical mixture of CN and KNO_3 was also prepared and named as CN-KN3-mixture.

2.2 Characterization

The crystal phases of the samples were analyzed by X-ray diffraction (XRD) with Cu Kα radiation (model D/max RA, Rigaku Co., Japan). X-ray photoelectrons spectroscopy (XPS) with Al Kα X-rays (hν = 1486.6 eV) radiation operated at 150 W (Thermo ESCALAB 250, USA) was used to investigate the surface properties. Scanning electrons microscopy (SEM, model JSM-6490, Japan) and transmission electrons microscopy (TEM, JEM-2010, Japan) were used to characterize the morphology and structure. Nitrogen adsorption-desorption isotherms were obtained on a nitrogen adsorption apparatus (ASAP 2020, U.S. A.) with all samples degassed at 300 ℃ for 4 h before measurements. Electrons spin resonance (ESR) of radicals spin-trapped by 5, 5-dimethyl-1-pyrroline N-oxide (DMPO) was recorded on a JES FA200 spectrometer. Samples for ESR measurement were prepared by mixing the samples in a 50 mM DMPO solution tanks (aqueous dispersion for DMPO-•OH and methanol dispersion for DMPO-•O_2^-) and irradiated with visible-light. Electrons paramagnetic resonance (EPR) measurements were carried out on a Bruker ESP 500 spectrometer. Steady and time-resolved fluorescence emission spectra were recorded

at room temperature with a fluorescence spectrophotometer (Edinburgh Instruments, FLSP-920). Photoluminescence (PL) studies (F-7000, HITACHI, Japan) and the UV-vis diffuse-reflectance spectrometry (UV-vis DRS) spectra which were obtained for the dry-pressed disk samples using a scanning UV-vis spectrophotometer (UV-vis DRS, UV-2450, Shimadzu, Japan) equipped with an integrating sphere assembly were obtained to investigate the optical properties of the samples.

2.3 DFT Calculations

Density functional theory (DFT) calculations were carried out using the "Vienna *ab initio* simulation package" (VASP5.3.5) [24], applying a generalized gradient correlation functional [25]. A plane-wave basis set with cut-off energy 400 eV within the framework of the projector-augmented wave method was employed [26, 27]. The Gaussian smearing width was set to 0.2 eV. The Brillouin zone was sampled with a 3 × 3 × 1 Monkhorst Pack grid. All atoms were converged to 0.01 eV/Å. The *ab initio* molecular dynamics (AIMD) were carried out to verify the thermostability of doped configurations, using *Born-Oppenheimer* approximation [28, 29]. A 2 × 2 × 3 supercell of bulk CN was first relaxed, then K atom was introduced in interlayer of CN and NO_3^- species were introduced in plane or interlayer of CN (Fig. S1c, d). In addition, the model of K atoms intercalated in interlayer of CN and NO_3^- species placed in plane or interlayer of CN also calculated for comparison.

The doping energy (E_d) is defined as

$$E_d = E_{doped\ CN} - (E_{pure\ CN} + E_{species}) \quad (1)$$

where $E_{species}$ refers to the total energy of K and KNO_3 species, which is calculated

from its respective unit cell.

The adsorption energy (E_{ads}) is defined as

$$E_{ads} = E_{tot} - (E_{CN} + E_{mol}) \quad (2)$$

where E_{tot}, E_{CN} and E_{mol} depict the total energy of the adsorption complex, the pure CN and the isolated molecule, respectively.

2.4 In situ DRIFTS investigation

In situ DRIFTS measurements were conducted using a TENSOR II FT-IR spectrometer (Bruker) equipped with an in situ diffuse-reflectance cell (Harrick) and a high-temperature reaction chamber (HVC), as shown in Scheme S1. The reaction chamber was equipped with three gas ports and two coolant ports. High-purity He, high-purity O_2, and 100 ppm of NO (in He) mixtures could be fed into the reaction system, and a three-way ball valve was used to switch between the target gas (NO) and purge gas (He). The total gas flow rate was 100 mL/min, and the concentration of NO was adjusted to 50 ppm by dilution with O_2. The chamber was enclosed with a dome having three windows, two for IR light entrance and detection, and one for illuminating the photocatalyst. The observation window was made of UV quartz and the other two windows were made of ZnSe. A Xe lamp (MVL-210, Japan) was used as the irradiation light source. Before measurements, prepared samples were pretreated 20 min at 300 °C.

2.5 Visible-light photocatalytic NO removal

The photocatalytic activity was investigated by the removal ratio of NO at ppb levels (500 ppb) in a continuous-flow reactor (rectangular reactor, 30 cm × 15 cm ×

10 cm). The concentration of NO was continuously detected by a NO_X analyzer (Thermo Environmental Instruments Inc., model 42c-TL), which can monitor the concentration of NO, NO_2 and NO_X (NO_X represents NO + NO_2). The as-prepared sample (0.20 g) was dispersed and coated onto two glass dishes (12.0 cm in diameter) for photocatalytic activity tests. A 150 W commercial tungsten halogen lamp was vertically placed outside and above the reactor and the lamp was turned on when the adsorption-desorption equilibrium was achieved. The removal ratio (η) of NO was calculated as $\eta = (1 - C/C_0) \times 100\%$, where C and C_0 are the concentrations of NO in the outlet steam and the feeding stream, respectively.

3. Results and discussions

3.1 Electronic structure and microstructure

Fig. 1

As revealed by the XRD pattern in Fig. 1a, the formation of CN polymer is indicated by the two characteristic diffraction peaks at 13.1° and 27.2°, which arise from the in-plane structural repeating motifs of the aromatic systems and the interlayer reflection of a graphite-like structure, respectively [30, 31]. Particularly, there are no impurity peaks and peaks of KNO_3 detected, suggesting that KNO_3 doped into CN interlayers by the form of potassium species (K^+) and nitrate species (NO_3^-). Correspondingly, a down-shift of the (002) peak over CN-KN samples has been observed in comparison with pristine CN, which can be ascribed to the intercalation of KNO_3 into the interlayers to expand the crystal lattice.

Next, XPS was applied to elaborate the chemical composition and valence states of the elements. The typical high-resolution C 1*s* and N 1*s* XPS spectra of CN and

CN-KN3 are shown in Fig. S1. Obviously, binding energies located at 293.03 and 295.7 eV, which are corresponding to the K $2p_{3/2}$ and K $2p_{1/2}$ peaks of K element in CN-KN3 (Fig. 1b), demonstrate K^+ has been successfully doped into CN. Because the pristine CN contains the N and O elements and the doping level of KNO_3 are very low, NO_3^- is hard to be detected by experimental methods.

In order to certify the introduction of NO_3^-, the direct AIMD simulation evidence is further provided to identify the thermal stability of NO_3^- at the specific temperature window and simultaneously explore the doping sites of NO_3^- in CN. As shown in Fig. 2c, the equilibrium bond length of N-O bond in NO_3^- hardly fluctuates at 800 and 900 K, indicating that the NO_3^- are quite stable and hard to be thermally decomposed during the co-pyrolysis preparation. In addition, NO_3^- can regularly move back and forth between neighboring CN layers and the average distance are about 2.23 Å, 2.36 Å at 800 and 900 K respectively, which are obviously shorter than the interlayered distance of CN (3.68 Å, Fig. 1g). Hence it is confirmed that NO_3^- could be intercalated into the space between the CN layers. Besides, the increased oxygen content of CN-KN3 in Fig. 1d are attributed to the NO_3^-, which also indicates the insertion of NO_3^-. Accordingly, the KNO_3 co-doped CN can be synthesized by a facile co-pyrolysis method.

Further, the deduction that KNO_3 tends to be intercalated into the interlayers ignites our interest to unravel how KNO_3 affected the geometric structures of CN at the atomic level and urges us to confirm it by DFT calculation. Based on our previous research, K^+ is inclined to be doped into the CN interlayers, which could enlarge the interlayer distance to make NO_3^- more easily enter into the interlayer space and enhance the coordination of NO_3^- with the surrounding K^+ [17]. So we build different crystal structures that K^+ are embedded in interlayer of CN and NO_3^- species are

placed in plane or interlayer of CN to determine the optimal doping sites for NO_3^-. According to the calculated results, NO_3^- species are preferably doped between the CN layers as the E_d of the intercalated structures (Fig. S2d) are obviously lower than that of the in-plane ones (Fig. S2c). So K^+ and NO_3^- can be stably co-intercalated in the adjacent CN layers. The optimized crystal structures are displayed in Fig. 1e-1g. The crystal structures of CN-K and CN-KN do not undergo obvious change *via* KNO_3 interaction but the layer distance is further enlarged, which is consistent with the XRD analysis, indicating the successful interposition of KNO_3 in the interlayers.

Fig. 2

Table 1

The SEM and TEM images of CN and CN-KN3 are presented in Fig. 2. As shown in Fig. 2b, CN-KN3 with a layered structure can be observed, which is similar to the pristine CN (Fig. 2a). The N_2 adsorption-desorption isotherms (Fig. S3) of CN and CN-KN samples are of type IV and H3 hysteresis loops. This result indicates the formation of mesoporous structure created by curved and stacked nanosheets [32], which is further confirmed by the Barrett-Joyner-Halenda (BJH) pore-size distribution curves (Fig. S3). Obviously, the introduction of KNO_3 does not influence the microstructure of CN. And the relevant parameters of specific surface area (S_{BET}) and pore volume of samples are listed in Table 1. Additionally, EDX elemental mapping of CN-KN3 (Fig. 2c-2f) suggests that the C, N, K and O elements are distributed uniformly.

3.2 Visible light photocatalytic NO removal and reactive species trapping

Fig. 3

Subsequently, the photocatalytic performance of CN-KN samples were evaluated by removal of NO in air under visible-light irradiation ($\lambda > 420$ nm). As shown in Fig. 3a, the maximum NO removal ratios can be reached in *ca.* 5 min and all the CN-KN samples exhibit superior activity than that of the pristine CN (Table 1), indicating that KNO_3 co-doping is an effective strategy to advance the photocatalysis efficiency of CN. Note that the mechanical mixture sample (CN-KN3-mixture) shows lower photocatalytic activity, demonstrating the fabrication of CN-KN *via* a facile co-pyrolysis process is indispensable.

The reactive species responsible for photocatalytic NO removal and the reasons for enhanced photocatalytic activity have been investigated and elaborated by DMPO spin-trapping ESR. As expected, a much stronger DMPO-$\bullet O_2^-$ signals can be observed for CN-KN3 in comparison with CN (Fig. 3b). This improvement is associated with the improved electrons excitation property and the better charge transfer characteristic, which enables more molecular oxygen activated by electrons and subsequently generating more superoxide radicals ($\bullet O_2^-$) for photocatalysis.

Further, the mechanism for the enhanced production of $\bullet O_2^-$ is confirmed by DFT calculation. In comparison to the pristine CN, the E_{ads} of O_2 molecules increase from -0.21 eV of CN to -0.45 eV of CN-KN. The O-O band lengths are elongated from 1.24 to 1.40 Å, which indicates that the inset of KNO_3 between CN layers could accelerate the adsorption of O_2 molecule and then weaken the O-O bands. As a result, the O_2 molecules in CN-KN are activated and transformed into $^{\bullet}O_2^-$ via obtaining abundant electrons. Indeed, the total charge (Δq) of O_2, calculated with Bader method

[33], increased from −0.39 e (CN) to −0.80 e (CN-KN) with the incorporation of KNO_3. Therefore, these results imply that the increased electrons and the enhanced charge transfer characteristic of CN-KN could facilitate the production of $\bullet O_2^-$ radicals to participate in the photocatalytic redox reaction, in correspondence with the DMPO-$\bullet O_2^-$ results (Fig. 3b). Furthermore, the DMPO-•OH adduct signal is detected as well. Though the potential energy of the valence band (VB) holes (1.40 eV) from CN are more negative than the OH^-/•OH and H_2O/•OH potentials (1.99 and 2.37 eV) and cannot directly oxidize OH^-/H_2O into hydroxyl radicals (•OH), the observed •OH radicals in Fig. 3e can be formed through the reduction of $\bullet O_2^-$ *via* a route of $\bullet O_2^- \rightarrow H_2O_2 \rightarrow$ •OH, which also reflect the promoted electrons excitation and charge transfer properties of CN-KN3.

The photocatalytic performance is strongly related to the generation of reactive species, which is determined by the number of photogenerated electrons-hole pairs and the separation, transportation and transformation efficiency of carriers. The intercalation of KNO_3 could boost the separation and transportation efficiency of carriers, giving rise to abundant electrons served for activating O_2 molecule. Consequently, there are more reactive species generated to participate in the photocatalytic redox reaction, which endows the CN-KN a superior visible-light photocatalytic performance. Therefore, further exploration of the promoted separation, transportation and transformation efficiency of charge carriers *via* KNO_3 intercalation should be carried out to elaborate the essentials for the enhanced photocatalytic performance.

3.3 Charge separation, transportation and transformation

Fig. 4

Electronic properties of pristine CN and the optimized CN-KN3 were examined by room temperature solid state electrons paramagnetic resonance (EPR). As shown in Fig. 4a, only one single Lorentzian line centered at a g value of 2.0 is detected, originating from unpaired electrons on π-conjugated CN aromatic rings [16, 34, 35]. The EPR signal intensity of CN-KN3 is stronger than that of pure CN both in dark and under visible-light irradiation, indicating that the intercalation of KNO_3 could widen the band distribution, boost the electrons mobility and accelerate the charge transportation.

Still, the direction and route of electrons transfer need to be further defined. Projected density of states (PDOS) is thus calculated (Fig. 4b). In comparison to the pristine CN, an obvious right−shift of N 2p electrons for CN-KN can be observed, which indicates that the electrons of N atoms in CN-KN possess a higher energy level to approach the valence band maximum. This could induce the carriers to be photoexcited easily under visible-light irradiation. Simultaneously, the mobility of electrons has been boosted, consistent with the EPR results. Notably, this right-shift is dominantly donated by the electrons migration along the Z direction (i. e. the direction vertical to CN planes), which implies that the delocalized π bonds have been extended to deviate from the planes (the X and Y directions), resulting in the promotion of the electrons transfer towards the Z direction. Therefore, the potential vertical electrons transportation channels between the adjacent CN layers could be constructed by

KNO_3 intercalation.

Fig. 5

Furthermore, Fig. 5a depicts the electrostatic potentials of CN, CN-K and CN-KN between adjacent CN layers. The valley bottom denotes the position of CN layer, and the highest peak position signifies the lowest energy barriers that electrons need to stride over the layers. As shown in Fig. 5a, a large potential barrier about -34.16 eV prohibits the transport of charge carriers between the adjacent layers (CN). Differently, the electrostatic potential between the first layer (L1) and second layer (L2) of CN is greatly increased after K^+ doping (CN-K). Significantly, with the co-doping of KNO_3 (CN-KN), the electrostatic potential is further elevated from -30.48 eV of CN-K to -28.17 eV of CN-KN. Such decreased energy barriers could promote the electrons transfer towards the Z direction readily, which makes the construction of the interlayer electrons delivery channels become feasible.

The charge difference distribution is provided to intuitively illustrate the gain or loss of electrons between the adjacent layers and reveal the charge transfer direction. As shown in Fig. 5b, the intercalation of K and KNO_3 both make the charge redistribute between adjacent layers, which decrease the electrons delocalization and extend the π conjugated systems to deviate from the planes. So the random electrons migration becomes oriented and transfers towards the Z direction. As similar to our previous research [17], K^+ could chemically bond with N (C) atoms at the neighboring layers to bridge the layers and form interlayer electrons delivery channel (electrons delivery direction is from L1 to L2). Notably, in the case of CN-KN, apart

from the electrons delivery channel formed by K^+, N (C) atoms (in L2) close to the interbedded NO_3^- could donate electrons to NO_3^- to steer the electrons transfer from L2 to L1, resulting in the formation of another vertical electrons transportation channel with electrons delivery direction from L2 to L1.

This interlayer bi-oriented electrons transportation channels by sandwiching K^+ and NO_3^- species between CN layers could significantly reduce the energy barriers for electrons transfer between adjacent layers and drive the charge flow in the two different channels but with opposite directions. Thus, the inevitable recombination of carriers which caused by the accumulation of electrons in one layer through single channel transportation have been precluded and then the separation and transportation efficiency of carriers has been dramatically boosted. Consequently, the abundant electrons in the channels could directly activate O_2 molecule to generate abundant reactive species for the photocatalytic redox reaction. Simultaneously, the prolonged radiative lifetime from 2.09 ns for CN to 2.23 ns for CN-KN3 and the quenching of PL peaks of CN-KN3 (Fig. 5c, 5d) further confirm that the recombination of electrons-hole pairs have been largely inhibited, demonstrating the formation of bi-oriented transportation channels, as a new strategy, could enhance the separation and transportation of carriers effectively.

3.4 Optical property and band structure

Fig. 6

The light adsorption property of the as-prepared catalysts is investigated by combined experimental and theoretical approach. As shown in UV-Vis DRS spectra

(Fig. 6a, Experiment), in contrast to the pristine CN, the intercalation of KNO_3 enables the red-shift of optical absorption band edge. Meanwhile, the calculated adsorption spectra are presented (Fig. 6a, Calculation), displaying the right-shift of absorption edges for CN-KN, which is in agreement with the experimental result. So, the intercalation of KNO_3 could broaden the absorption range in visible-light region and narrow the band gap of CN.

The density of states (DOS) are calculated and displayed in Fig. 6b. The total DOS shows that the band gap of pure CN is 0.72 eV. It is smaller than that of the experimental value, which is due to the known limitation of plain DFT method [36]. In contrast, CN-KN displays narrowed band gap, which indicate that the higher visible-light absorption ability of CN-KN has been endowed, consistent with the observation in Fig. 6a. Additionally, the valence band (VB) and conduction band (CB) edges of the CN-K and CN-KN are down-shift relative to those of bare CN. Thus the band structure of CN can be well-tailored by the intercalation of KNO_3.

Concretely, the extra lone-pair electrons of the two-coordinated N atoms in CN are significantly delocalized *via* sandwiching KNO_3 between adjacent layers to generate the interlayered channels, which lead to the electrons hopping from higher energy level to lower one, hence contributing to the down-shift of band edge and narrowed band gap. Therefore, the CN-KN not only possesses a narrower band gap but also higher oxidization ability of VB holes than pure CN, resulting in an expected elevated photocatalytic activity for NO removal.

3.5 In situ DRIFTS investigation and photocatalysis reaction mechanism

Fig. 7

To intuitively reveal the conversion pathways and reaction mechanism of photocatalytic NO oxidation with CN and CN-KN3, *in situ* DRIFTS were carried out to dynamically monitor the reaction intermediates and products over the photocatalysts surface in time sequence (Fig. 7). The background spectrum is recorded before NO is injected into the reaction chamber. The NO absorption bands appear once the NO contacts the photocatalyst at 25 ^{o}C in dark condition (Fig. 7a, 7b). On the surface of CN, the absorption bands of N_2O (2283, 2234 and 2176 cm^{-1}), NO_2 (2087 cm^{-1}), N_2O_3 (960 cm^{-1}) and N_2O_4 (910 cm^{-1}) have been detected, which is due to the chemical adsorption of NO on CN [37-40]. Over time, the intensity of absorption band at 2176, 2087 and 910 cm^{-1} are increased progressively, indicating the gradual accumulation of nitro compounds on CN. And the other developed absorption bands can be assigned to the stretching vibration of bidentate nitrito (1208 cm^{-1}), bidentate nitrates (1120-1030 cm^{-1}), monodentate nitrite or chelated nitrite (870 cm^{-1}) [37, 38, 41-43], arising from the active two-coordinated N atoms which could facilitate the formation of the activated oxygen species that enhance the oxidation capacity of surface oxygen species for NO_x oxidation [44, 45]. The observed IR bands of the adsorbed species and their chemical assignments are listed in Table S1-S4.

In the case of CN-KN3, the assignment of adsorption peaks is similar to that of NO adsorption over pristine CN. But one notable difference is that an obvious band associated with NO^+ appeared at 2150 cm^{-1} (Fig. 7b), which is proven to be the

reaction intermediate of NO oxidation [38, 46-49]. Hadjiivanov et al. found that when NO is adsorbed on surfaces possessing strongly oxidative properties, the NO oxidation product (NO^+) is usually observed [50]. Thus the NO adsorbed on CN-KN3 may partly exchange with K^+, leading to the formation of NO^+ and simultaneous reduction of cationic sites. The adsorbed NO^+ as the reaction intermediates would be preferentially oxidized to nitro compounds by reactive oxygen species compared with other nitrogen-containing species [48, 49]. Hence the sandwiched K^+ species could greatly promote the conversion of NO to final products.

After achieving the adsorption equilibrium, the time-dependent IR spectra of CN and CN-KN under visible-light irradiation are recorded dynamically. The spectrum of "Ads. Equil" is the same as that of "NO + O_2 20 min" in the adsorption process. As shown in the photocatalytic NO oxidation process over CN (Fig. 7c), the adsorption intensity of the intermediates (N_2O, NO_2, N_2O_3 and N_2O_4) and final products (nitrites, nitrates) during photocatalysis is observably increased. Besides, new absorption bands at 1127, 1003, 987, 885 cm^{-1} were detected, which can be attributed to the final products of photocatalytic NO oxidation (bidentate NO_2^-, bridging nitrates, chelating bidentate NO_3^- species and NO_2^-, respectively) [37, 40, 46, 51]. These final products accumulated on the photocatalyst surface can be easily removed by water washing and the photocatalyst can be regenerated via this facile method.

Correspondingly, the time-dependent IR spectra of CN-KN3 are recorded and shown in Fig. 7d. In the range of 1260-830 cm^{-1}, the tendency of absorption bands is similar to CN. However, unlike the pure CN, adsorption bands of N_2O disappear,

indicating that the photocatalytic oxidation is improved. This can be ascribed to that the increased active radicals (Fig. 3b and 3d) facilitate the consumption of accumulated adsorption species via chemical reactions between them. Also, it must be mentioned that the adsorption band of NO^+ over CN-KN dies out during the visible-light irradiation but emerges again after turning off the light. This fact not only certifies the successful intercalation of KNO_3 into CN but also demonstrates the importance of photogenerated carriers for photocatalysis. Therefore, the intercalation of KNO_3 realizes the construction of interlayer bi-oriented electrons transportation channels to lower the interlayer energy barrier and steer interlayer charge flow for enhancing the separation and transportation efficiency of carriers and simultaneously could facilitate the activation of NO via the formation of NO^+ to promote the oxidation of NO for elevating the photocatalytic oxidation performance.

Fig. 8

Consequently, the time-dependent IR spectra illuminate the conversion pathway of photocatalytic NO oxidation and further reveal the essentials of the activity promotion mechanism. The roles of the bi-oriented electrons transportation channels in KNO_3 co-doped CN and the mechanism of photocatalytic NO oxidation are illustrated in Fig. 8.

4. Conclusion

With a highly combined theoretical and experimental approach, we have demonstrated that constructing interlayer bi-oriented electrons transportation channels

in CN via intercalation KNO_3 species between neighboring layers is a novel and efficient strategy to enhance photocatalytic performance. The established bi-oriented channels could reduce the energy barriers for electrons transfer between adjacent layers and drive the charge flow towards opposite directions. Consequently, the separation and transportation efficiency of carriers are significantly boosted, resulting in abundant electrons provided to activate O_2 molecule and thus dramatically facilitates the production of reactive species to participate in the photocatalytic redox reaction. The reduced energy barrier, promoted charge separation and transportation, and enhanced O_2 molecule activation of CN-KN in all contributed to the highly enhanced visible-light photocatalytic performance in NO purification. The time-dependent *in situ* IR spectra in conjunction with ESR spectra and DFT calculation revealed the conversion pathway of photocatalytic NO oxidation and photocatalytic promotion mechanism. This research sheds atomic-level insights into steering the interlayer energy barrier and charge flow *via* a desired and efficient manner, thus opening up a new vista to explore and design high-performance layered photocatalysts for practical applications.

Acknowledgments

This research was financially supported by National Natural Science Foundation of China (51478070, 21501016 and 51108487), the National Key R&D project (2016YFC0204702), and the Innovative Research Team of Chongqing

(CXTDG201602014).

References

[1] H. Tong, S. Ouyang, Y. Bi, N. Umezawa, M. Oshikiri, J. Ye, Nano-photocatalytic materials: possibilities and challenges, Adv. Mater. 24 (2012) 229-251.

[2] Y. Ma, X. Wang, Y. Jia, X. Chen, H. Han, C. Li, Titanium dioxide-based nanomaterials for photocatalytic fuel generations, Chem. Rev. 114 (2014) 9987-10043.

[3] H. Wang, L. Zhang, Z. Chen, J. Hu, S. Li, Z. Wang, J. Liu, X. Wang, Semiconductor heterojunction photocatalysts: design, construction, and photocatalytic performances, Chem. Soc. Rev. 45 (2014) 5234-5244.

[4] J. Zhang, M. Zhang, S. Lin, X. Fu, X. Wang, Molecular doping of carbon nitride photocatalysts with tunable bandgap and enhanced activity, J. Catal. 310 (2014) 24-30.

[5] L. G. Devi, R. Kavitha, A review on non metal ion doped titania for the photocatalytic degradation of organic pollutants under UV/solar light: Role of photogenerated charge carrier dynamics in enhancing the activity, Appl. Catal. B 140-141 (2013) 559-587.

[6] P. Zhang, T. Wang, X. Chang, J. Gong, Effective charge carrier utilization in photocatalytic Conversions, Acc. Chem. Res. 49 (2016) 911-921.

[7] F. Dong, T. Xiong, S. Yan, H. Wang, Y. Sun, Y. Zhang, H. Huang, Z. Wu, Facets and defects cooperatively promote visible light plasmonic photocatalysis with Bi nanowires@BiOCl nanosheets, J. Catal. 344 (2016) 401-410.

[8] K. S. Novoselov, A. Mishchenko, A. Carvalho, A. H. Castro Neto, 2D materials and van der Waals heterostructures, Science 353 (2016) aac9439.

[9] Q. Fu, X. Bao, Surface chemistry and catalysis confined under two-dimensional materials, Chem. Soc. Rev. 46 (2016) 1842-1874.

[10] B. Luo, G. Liu, L. Wang, Recent advances in 2D materials for photocatalysis, Nanoscale 8 (2016) 690406920.

[11] J. Di, J. Xia, H. Li, Z. Liu, Freestanding atomically-thin two-dimensional materials beyond graphene meeting photocatalysis: opportunities and challenges, Nano Energy 35 (2017) 79-91.

[12] X. Wang, K. Maeda, A. Thomas, K. Takanabe, G. Xin, J. M. Carlsson, K. Domen, M. Antonietti, A metal-free polymeric photocatalyst for hydrogen production from water under visible light, Nat. Mater. 8 (2009) 76-80

[13] W. J. Ong, L. L. Tan, H. N. Yun, S. T. Yong, S. P. Chai, Graphitic carbon nitride ($g\text{-}C_3N_4$)-based photocatalysts for artificial photosynthesis and environmental remediation: are we a step closer to achieving sustainability?, Chem. Rev. 116 (2016) 7159-7329.

[14] A. Thomas, A. Fischer, F. Goettmann, M. Antonietti, J. O. Mueller, R. Schloegl, J. M. Carlsson, ChemInform abstract: graphitic carbon nitride materials: variation of structure and morphology and their use as metal-free catalysts, J. Mater. Chem. 40 (2009) 4893-4908.

[15] S. Cao, Y. Li, B. Zhu, M. Jaroniec, J. Yu, Facet effect of Pd cocatalyst on photocatalytic CO_2 reduction over $g\text{-}C_3N_4$, J. Catal. 349 (2017) 208-217.

[16] G. Zhang, M. Zhang, X. Ye, X. Qiu, S. Lin, X. Wang, Iodine modified carbon nitride semiconductors as visible light photocatalysts for hydrogen evolution, Adv. Mater. 26 (2014) 805-809.

[17] T. Xiong, W. Cen, Y. Zhang, F. Dong, Bridging the g-C_3N_4 interlayers for enhanced photocatalysis, ACS Catal. 6 (2016) 2462-2472.
[18] Y. Kang, Y. Yang, L.C. Yin, X. Kang, L. Wang, G. Liu, H.M. Cheng, Selective breaking of hydrogen bonds of layered carbon nitride for visible light photocatalysis, Adv. Mater. 28 (2016) 6471-6477.
[19] Q. L. Tay, X. H. Wang, X. Zhao, J. D. Hong, Q. Zhang, R. Xu, Z. Chen, Enhanced visible light hydrogen production via a multiple heterojunction structure with defect-engineered g-C_3N_4 and two-phase anatase/brookite TiO_2, J. Catal. 342 (2016) 55-62.
[20] W.Chen, Y. Hua, Y. Wang, T. Huang, T. Liu, X. Liu, Two-dimensional mesoporous g-C_3N_4 nanosheet-supported $MgIn_2S_4$ nanoplates as visible-light-active heterostructures for enhanced photocatalytic activity, J. Catal. 349 (2017) 8-18.
[21] H. Gao, S. Yan, J. Wang, Y. A. Huang, P. Wang, Z. Li, Z. Zou, Towards efficient solar hydrogen production by intercalated carbon nitride photocatalyst, Phys. Chem. Chem. Phys. 15 (2013) 18077-18084.
[22] S. Z. Hu, L. Ma, J. G. You, F. J. Li, Z. P. Fan, G. Lu, D. Liu, J. Z. Gui, Enhanced visible light photocatalytic performance of g-C_3N_4 photocatalysts co-doped with iron and phosphorus, Appl. Surf. Sci. 311 (2014) 164-171.
[23] S. S. Shinde, A. Sami, J. H. Lee, Electrocatalytic hydrogen evolution using graphitic carbon nitride coupled with nanoporous graphene co-doped by S and Se, J. Mater. Chem. A 3 (2015) 12810-12819.
[24] G. Kresse, J. Furthmüller, J. Efficient iterative schemes for ab initio total-energy calculations using a plane-wave basis set, Phys. Rev. B: Condens. Matter Mater. Phys. 54 (1996) 11169-11186.
[25] J. P. Perdew, K. Burke, M. Ernzerhof, Generalized gradient approximation made simple, Phys. Rev. Lett. 77 (1996) 3865-3868.
[26] P. E. Blochl, Projector augmented-wave method, Phys. Rev. B 50 (1994) 17953-17979.
[27] G. Kresse, D. Joubert, From ultrasoft pseudopotentials to the projector augmented-wave method, Phys. Rev. B 59 (1999) 1758-1775.
[28] M. E. Tuckerman, Ab initio molecular dynamics: Basic concepts, current trends and novel applications, J Phys. Condens. Mat. 14 (2002) R1297.
[29] M. Born, W. Heisenberg, Zur quantentheorie der molekeln, Ann. Phys. 379 (1927) 1-31.
[30] F. Fina, S. K. Callear, G. M. Carins, J. T. S. Irvine, Structural Investigation of Graphitic Carbon Nitride via XRD and Neutron Diffraction, Chem. Mater. 27 (2015) 2612-2618.
[31] G. Zhang, J. Zhang, M. Zhang, X. Wang, Polycondensation of thiourea into carbon nitride semiconductors as visible light photocatalysts, J. Mater. Chem. 22 (2012) 8083-8091.
[32] K.S.W. Sing, Reporting physisorption data for gas/solid systems with special reference to the determination of surface area and porosity (Recommendations 1984), Pure Appl. Chem. 57 (2009) 603-619.
[33] Bader, R. Atoms in molecules: a quantum theory, Oxford University Press 1994.
[34] G. Zhang, X. Wang, A facile synthesis of covalent carbon nitride photocatalysts by co-polymerization of urea and phenylurea for hydrogen evolution, J. Catal. 307 (2013) 246-253.
[35] Z. A. Lan, G. Zhang, X. Wang, A facile synthesis of Br-modified g-C_3N_4 semiconductors for photoredox water splitting, Appl. Catal. B 192 (2016) 116-125.
[36] S. Steinmann, S. Melissen, T.L. Bahers, P. Sautet, Challenges in calculating the bandgap of triazine-based carbon nitride structures, J. Mater. Chem. A 5 (2017) 5115-5122.

[37] K. Hadjiivanov, V. Avreyska, A. Dimitar Klissurski, T. Marinova, Surface species formed after NO adsorption and NO + O_2 coadsorption on ZrO_2 and sulfated ZrO_2: an FTIR spectroscopic study, Langmuir 18 (2002) 1619-1625.

[38] J. C. S. Wu, Y. T. Cheng, In situ FTIR study of photocatalytic NO reaction on photocatalysts under UV irradiation, J. Catal. 237 (2006) 393-404.

[39] T. Weingand, S. Kuba, K. Hadjiivanov, H. Knözinger, Nature and reactivity of the surface species formed after NO adsorption and NO + O_2 coadsorption on a WO_3-ZrO_2 catalyst, J. Catal. 209 (2002) 539-546.

[40] L. Jaan, J.R. Ohlsen, Characterization of nitrogen oxides by vibrational spectroscopy, Prog. in Inorg. Chem. 27 (2007) 465-513.

[41] M. Kantcheva, A.S. Vakkasoglu, Cobalt supported on zirconia and sulfated zirconia I.: FT-IR spectroscopic characterization of the NO_X species formed upon NO adsorption and NO/O_2 coadsorption, J. Catal. 223 (2004) 352-363.

[42] Y. Zhou, Z. Zhao, F. Wang, K. Cao, D. E. Doronkin, F. Dong, J. D. Grunwaldt, Facile synthesis of surface N-doped $Bi_2O_2CO_3$: origin of visible light photocatalytic activity and in situ DRIFTS studies, J. Hazard. Mater. 307 (2016) 163-172.

[43] S.J. Huang, A.B. Walters, M.A. Vannice, Adsorption and decomposition of NO on lanthanum oxide, J. Catal. 192 (2000) 29-47.

[44] Y. Lin, D. Su, Fabrication of nitrogen-modified annealed nanodiamond with improved catalytic activity, ACS Nano 8 (2014) 7823-7833.

[45] J. Li, J. Liu, S. Yin, Y. Liu, J. Li, W. Cen, Y. Chu, Promoting mechanism of pyridine N doped carbocatalyst for SO_2 oxidation, RSC Adv. 6 (2016) 86316-86323.

[46] M. Kantcheva, dentification, stability, and reactivity of NO_x species adsorbed on titania-supported manganese catalysts, J. Catal. 204 (2001) 479-494.

[47] K. Hadjiivanov, H. Knozinger, Species formed after NO adsorption and NO + O_2 co-adsorption on TiO_2: an FTIR spectroscopic study, Phys. Chem. Chem. Phys. 2 (2000) 2803-2806.

[48] L. Zhong, Y. Yu, W. Cai, X. Geng, Q. Zhong, Structure-activity relationship of Cr/Ti-PILC catalysts using a pre-modification method for NO oxidation and their surface species study, Phys. Chem. Chem. Phys 17 (2015) 15036-15045.

[49] N. Tang, Y. Liu, H.Q. Wang, Z.B. Wu, Mechanism study of NO catalytic oxidation over MnOx/TiO_2 catalysts, J. Phys. Chem. C 115 (2011) 8214-8220.

[50] K.I. Hadjiivanov, Identification of neutral and charged N_XO_Y surface species by IR spectroscopy, Catal. Rev. 42 (2007) 71-144.

[51] G. Ramis, G. Busca, V. Lorenzelli, P. Forzatti, Fourier transform infrared study of the adsorption and coadsorption of nitric oxide, nitrogen dioxide and ammonia on TiO_2 anatase, Appl. Catal. 64 (1990) 243-257.

Figure captions

Fig. 1 Crystal structures of CN-KN. (a) XRD patterns of as-prepared samples and the enlarged profile of the (002) diffraction region (inset); (b) XPS spectra of K 2*p*; (c) the time evolution in 10 ps for N-O length of NO_3^- and the fluctuation distance of doped NO_3^- in CN interlayer at 800 and 900 K with AIMD simulation; the survey spectra of CN and CN-KN3 (d); the optimized local structures of individual CN (e), K (f), KNO_3 (g) doped CN. All the lengths and energies are given in Å, gray, blue, purple and red spheres represent C, N, K and O atoms, respectively. E_d stands for the doping energy, negative means heat release.

Fig. 2 Morphology and structure of the as-prepared samples. SEM and TEM images of CN (a) and CN-KN3 (b). FESEM-EDX elemental mapping of CN-KN3 (c-f).

Fig. 3 Evaluation and analysis of the visible-light photocatalytic performance of the as-prepared samples. Photocatalytic activity in NO removal (a); DMPO ESR spectra in dark and under visible-light irradiation ($\lambda \geq 420$ nm), respectively in methanol dispersion for $^{\bullet}O_2^-$ (b) and aqueous dispersion for $^{\bullet}OH$ (e). Optimized O_2 adsorption in CN (c) and CN-KN (d). E_{ads} and Δq stand for the adsorption energy and the total charge for O_2 molecules, negative means heat release. All lengths are given in Å and the colour coding of atoms remain the same as in Fig. 1.

Fig. 4 Analysis of electrons transportation. Room temperature solid state EPR spectra of CN and CN-KN3 (a); projected density of states (PDOS) of N atoms in CN layers (b), the Fermi level is set to 0 eV.

Fig. 5 Analysis of electrons mobility. electrostatic potential (a); charge difference

distribution between metal atoms and CN layers: charge accumulation is in blue and depletion in yellow and the colour coding of atoms remains the same as in Fig. 1. The isosurfaces are set to 0.005 eV $Å^{-3}$ (b); The ns-level time-resolved fluorescence spectra surveyed under at room temperature (c); photoluminescence spectra of the as-obtained samples (d).

Fig. 6 Light adsorption and band structure property of the as-prepared catalysts. The UV-vis spectra and the calculated adsorption spectra (a); density of states (DOS), the Fermi level is set to 0 eV (b).

Fig. 7 In situ IR spectra of NO adsorption and visible-light reaction processes over CN and CN-KN3.

Fig. 8 The illustration of roles of the bi-oriented electrons transportation channels in KNO_3 co-doped CN and the mechanism of photocatalytic NO oxidation.

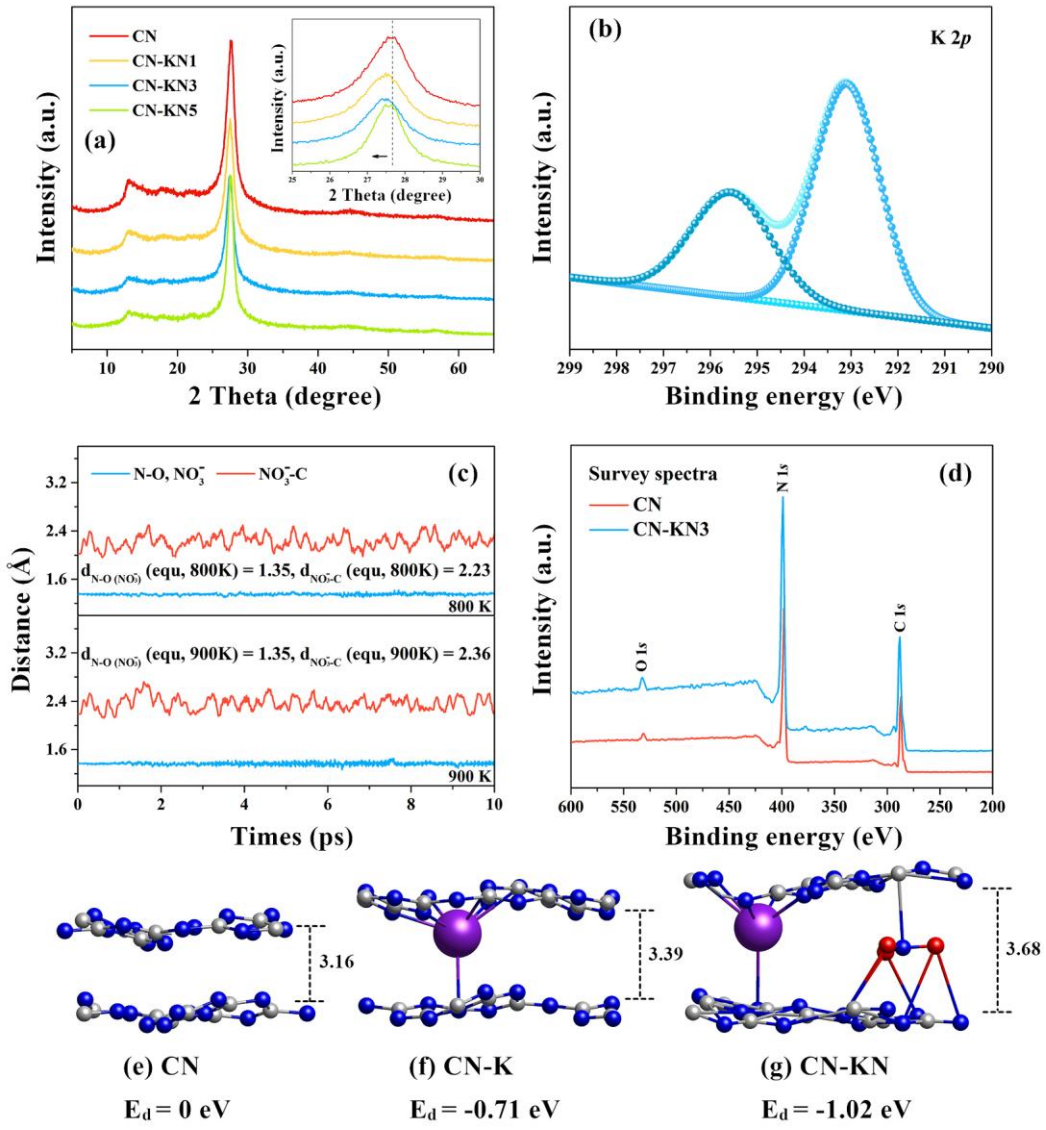

Fig. 1 Crystal structures of CN-KN. (a) XRD patterns of as-prepared samples and the enlarged profile of the (002) diffraction region (inset); (b) XPS spectra of K 2*p*; (c) the time evolution in 10 ps for N-O length of NO_3^- and the fluctuation distance of doped NO_3^- in CN interlayer at 800 and 900 K with AIMD simulation; the survey spectra of CN and CN-KN3 (d); the optimized local structures of individual CN (e), K (f), KNO_3 (g) doped CN. All the lengths and energies are given in Å, gray, blue, purple and red spheres represent C, N, K and O atoms, respectively. E_d stands for the doping energy, negative means heat release.

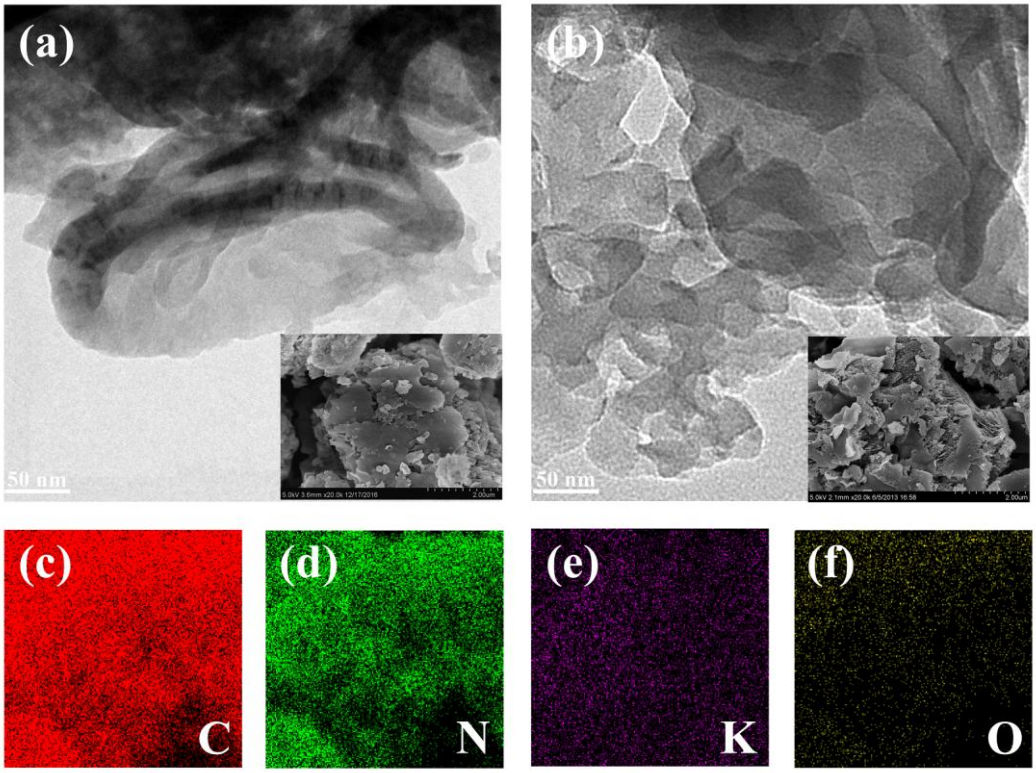

Fig. 2 Morphology and structure of the as-prepared samples. SEM and TEM images of CN (a) and CN-KN3 (b). FESEM-EDX elemental mapping of CN-KN3 (c-f).

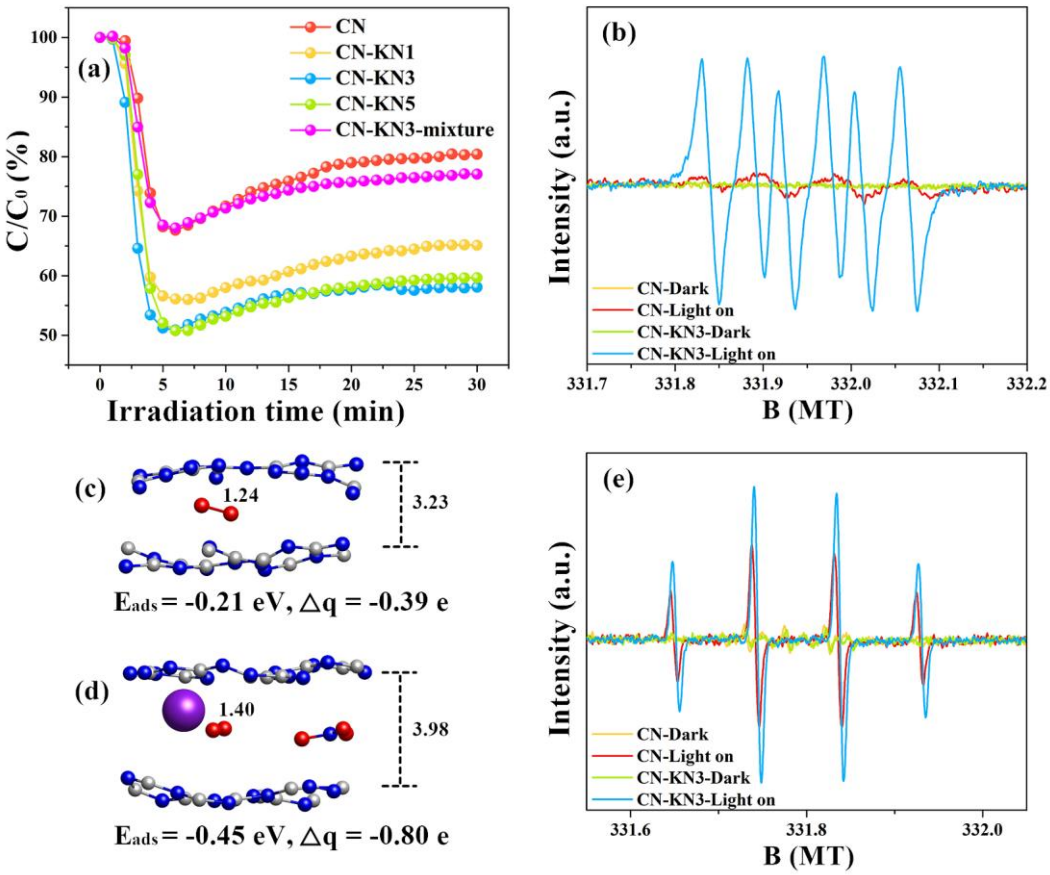

Fig. 3 Evaluation and analysis of the visible-light photocatalytic performance of the as-prepared samples. Photocatalytic activity in NO removal (a); DMPO ESR spectra in dark and under visible-light irradiation (λ≥420 nm), respectively in methanol dispersion for $^{\bullet}O_2^-$ (b) and aqueous dispersion for $^{\bullet}OH$ (e). Optimized O_2 adsorption in CN (c) and CN-KN (d). E_{ads} and Δq stand for the adsorption energy and the total charge for O_2 molecules, negative means heat release. All lengths are given in Å and the colour coding of atoms remain the same as in Fig. 1.

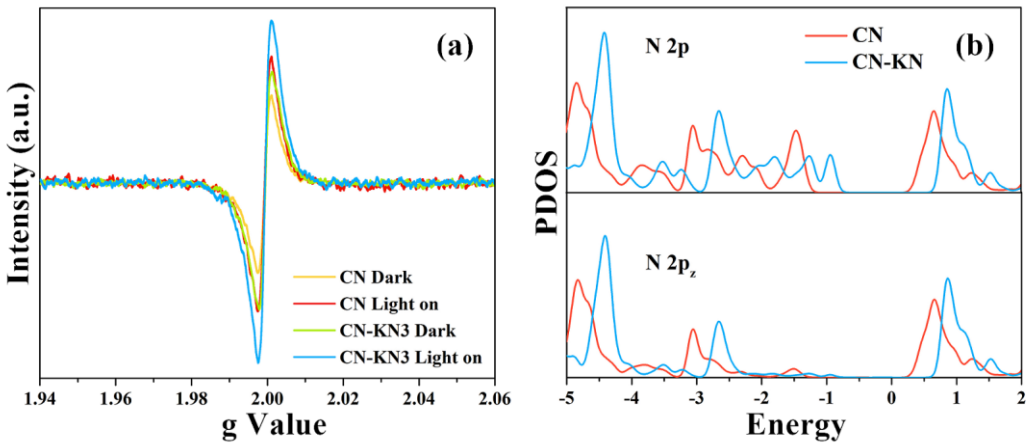

Fig. 4 Analysis of electrons transportation. Room temperature solid state EPR spectra of CN and CN-KN3 (a); projected density of states (PDOS) of N atoms in CN layers (b), the Fermi level is set to 0 eV.

5

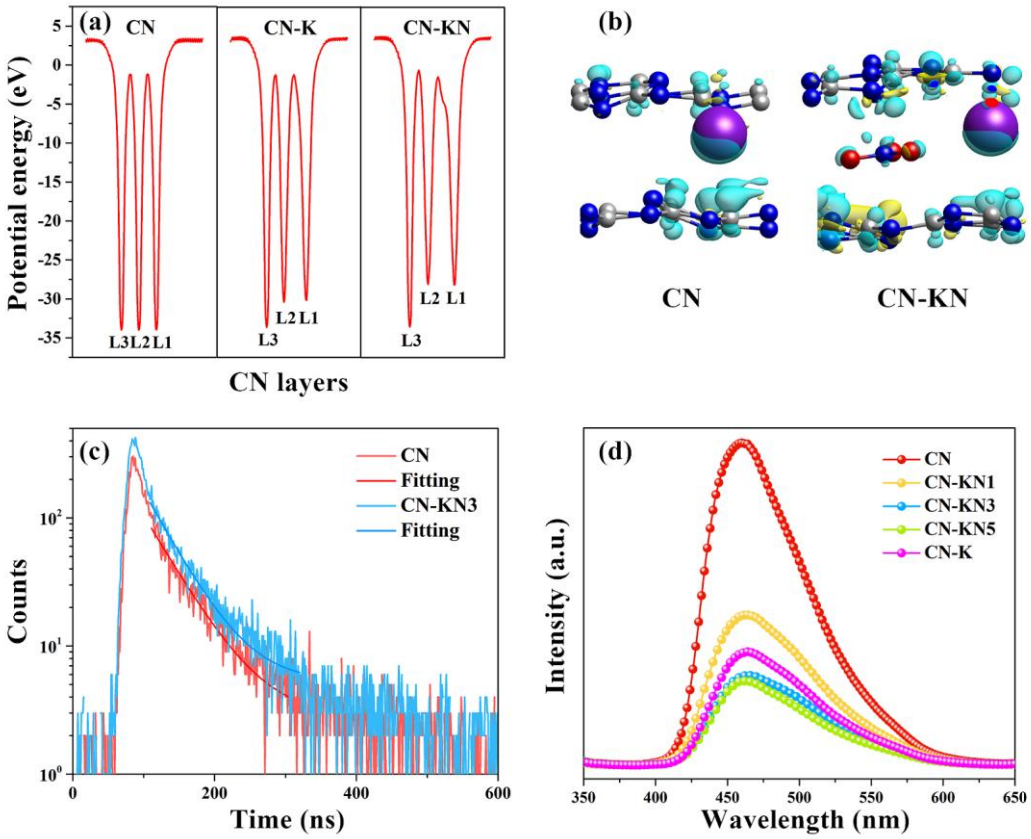

Fig. 5 Analysis of electrons mobility. electrostatic potential (a); charge difference distribution between metal atoms and CN layers: charge accumulation is in blue and depletion in yellow and the colour coding of atoms remains the same as in Fig. 1. The isosurfaces are set to 0.005 eV $Å^{-3}$ (b); The ns-level time-resolved fluorescence spectra surveyed under at room temperature (c); photoluminescence spectra of the as-obtained samples (d).

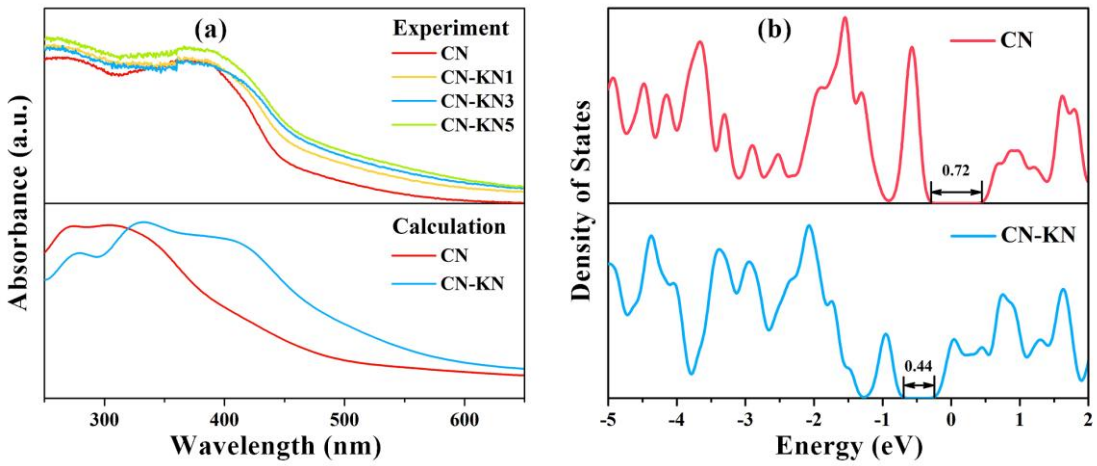

Fig. 6 Light adsorption and band structure property of the as-prepared catalysts. The UV-vis spectra and the calculated adsorption spectra (a); density of states (DOS), the Fermi level is set to 0 eV (b).

5

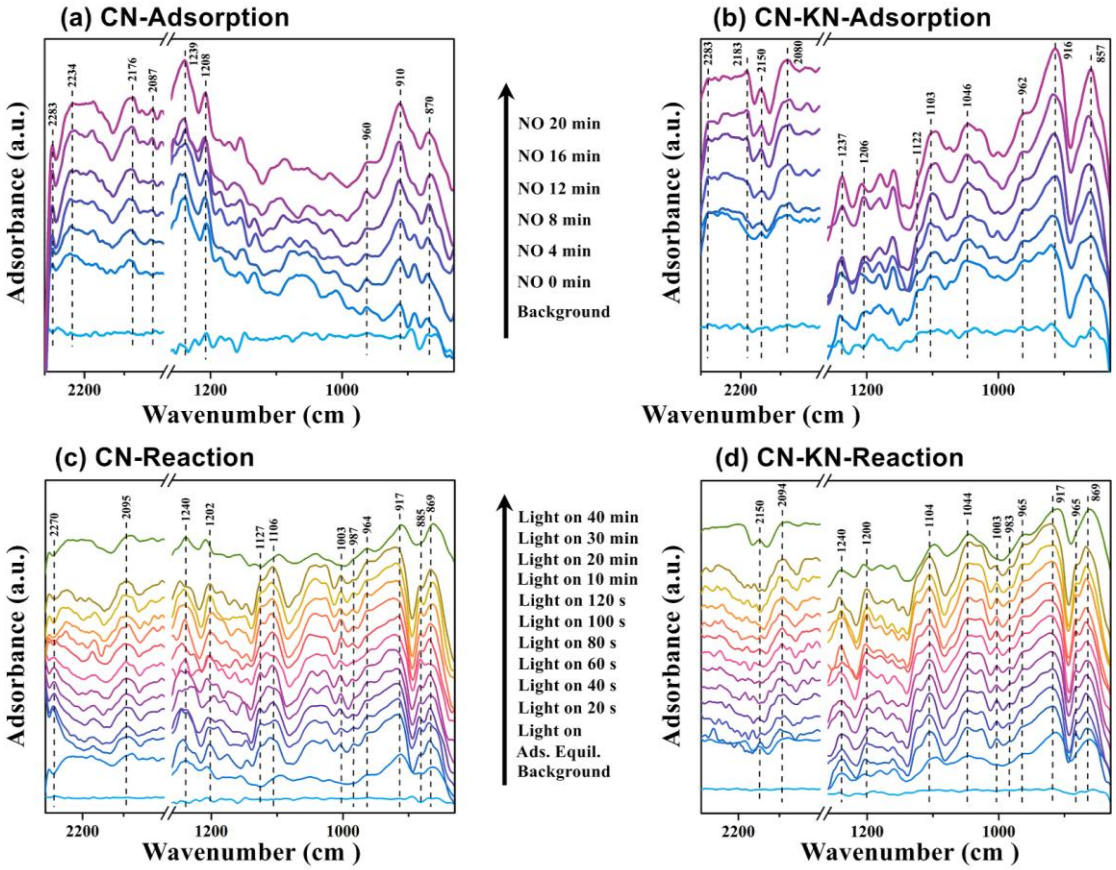

Fig. 7 In situ IR spectra of NO adsorption and visible-light reaction processes over CN and CN-KN3.

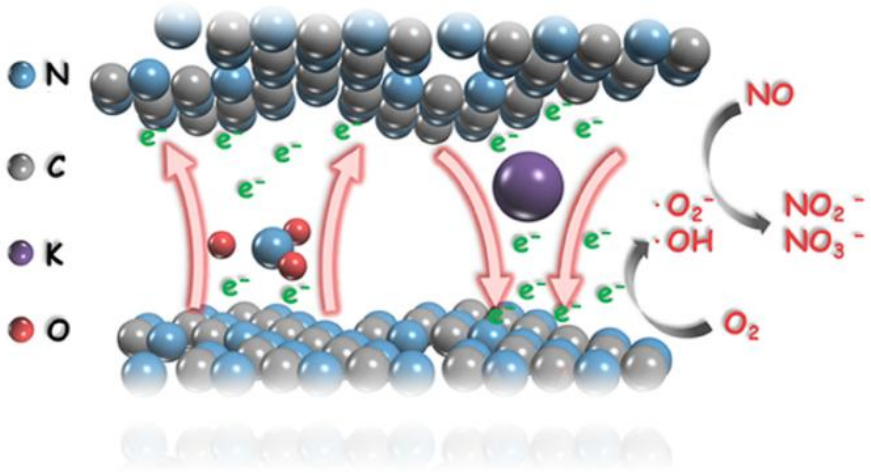

Fig. 8 The illustration of roles of the bi-oriented electrons transportation channels in KNO_3 co-doped CN and the mechanism of photocatalytic NO oxidation.

5

Table 1 NO removal ratio, specific surface area (S_{BET}), pore volume and fluorescence lifetime for individual, and KNO_3 doped CN, at different doping content.

Sample	η, %	S_{BET}, m^2/g	pore volume, cm^3/g	lifetime (τ1), ns
CN	19.60	26.82	0.17	2.09
CN-KN1	34.90	17.26	0.05	-
CN-KN3	41.93	13.31	0.08	2.23
CN-KN5	40.33	8.41	0.06	-
CN-KN3-mixture	22.95	23.22	0.14	-